Impact of Stroma on the Growth, Microcirculation, and Metabolism of Experimental Prostate Tumors

Christian M. Zechmann, Eva C. Woenne[†,‡], Gunnar Brix[§], Nicole Radzwill[¶], Martin Ilg[¶], Peter Bachert[‡], Peter Peschke[#], Stefan Kirsch[‡], Hans-Ulrich Kauczor*, Stefan Delorme*, Wolfhard Semmler[‡] and Fabian Kiessling[†,‡]*

*Department of Radiology, German Cancer Research Center (DKFZ), Heidelberg, Germany; [†]Junior Group Molecular Imaging, German Cancer Research Center (DKFZ), Heidelberg, Germany; [‡]Department of Medical Physics in Radiology, German Cancer Research Center (DKFZ), Heidelberg, Germany; [§]Department of Medical Radiation Hygiene and Dosimetry, Federal Office for Radiation Protection, Neuherberg, Germany; [¶]Bruker BioSpin MRI GmbH, Ettlingen, Germany; [#]Clinical Cooperation Unit Radiotherapy, German Cancer Research Center (DKFZ), Heidelberg, Germany

Abstract

In prostate cancers (PCa), the formation of malignant stroma may substantially influence tumor phenotype and aggressiveness. Thus, the impact of the orthotopic and subcutaneous implantations of hormone-sensitive (H), hormone-insensitive (HI), and anaplastic (AT1) Dunning PCa in rats on growth, microcirculation, and metabolism was investigated. For this purpose, dynamic contrast-enhanced magnetic resonance imaging and ^{1}H magnetic resonance spectroscopy ([^{1}H]MRS) were applied in combination with histology. Consistent observations revealed that orthotopic H tumors grew significantly slower compared to subcutaneous ones, whereas the growth of HI and AT1 tumors was comparable at both locations. Histologic analysis indicated that glandular differentiation and a close interaction of tumor cells and smooth muscle cells (SMC) were associated with slow tumor growth. Furthermore, there was a significantly lower SMC density in subcutaneous H tumors than in orthotopic H tumors. Perfusion was observed to be significantly lower in orthotopic H tumors than in subcutaneous H tumors. Regional blood volume and permeability–surface area product showed no significant differences between tumor models and their implantation sites. Differences in growth between subcutaneous and orthotopic H tumors can be attributed to tumor–stroma interaction and perfusion. Here, SMC, may stabilize glandular structures and contribute to the maintenance of differentiated phenotype.

Neoplasia (2007) **9,** 57–67

Keywords: Prostate cancer, microenvironment, angiogenesis, dynamic contrast-enhanced MRI, [^{1}H]NMR spectroscopy.

Introduction

Autopsy studies indicate that almost 30% of all men older than 50 years show microscopic prostate cancers (PCa) [1,2]. However, in contrast to most other malignant tumors, there is a high discrepancy between prevalence and mortality, and < 10% of men with PCa suffer from symptomatic disease during their lifetime [3]. About 29% of white men and 44% of black men are estimated to be overdiagnosed and overtreated [4]. Thus, there is an essential demand to distinguish aggressive PCa requiring therapeutic intervention from low malignant tumors, which will not become symptomatic.

Germline mutations leading to the dedifferentiation of normal prostate epithelium into androgen-independent PCa have been identified. The final step from localized PCa to metastatic phenotype is accompanied by androgen receptor changes and specific gene amplifications and losses [5]. Compared with their primary tumors, metastases are frequently marked by a faster and more infiltrative growth [6]. Besides genetic changes, the degree to which the heterotopic localization of metastases additionally influences phenotypic changes between primary tumors and metastases is poorly understood. This may be related to further selection of more resistant and aggressive subclones, the interaction of tumor cells with the surrounding fibroblastic stroma, and the development of neovascularization [7,8].

Experiments performed by Cunha et al. [7] and Hayward et al. [9] demonstrated that there is an epithelial–mesenchymal interaction in PCa development and that normal epithelial cells can be transformed by their microenvironment. Thus, aberrant interactions are most likely relevant in PCa development, and their investigation in experimental PCa may provide promising options for diagnosis and therapy.

Abbreviations: Cho, choline and choline-containing compounds; Ci, citrate; Cr, creatine and phosphocreatine; DCE-MRI, dynamic contrast-enhanced magnetic resonance imaging; FOV, field of view; [^{1}H]MRS, ^{1}H magnetic resonance spectroscopy; Lip, lipids; MA, matrix size; PCa, prostate cancers; PRESS, point-resolved spectroscopy; RBF, regional blood flow (perfusion); RBV, regional blood volume; PS/V_p, permeability–surface area product per unit of vascular volume (vessel permeability); SMA, smooth muscle actin; SMC, smooth muscle cells; T_H, slice thickness; T_E, echo time; T_R, repetition time; T_{REC}, recovery time; TSE, turbo spin echo; TUNEL, terminal deoxyribosyl transferase–mediated dUTP nick end labeling

Address all correspondence to: Fabian Kiessling, Junior Group Molecular Imaging, Im Neuenheimer Feld 280, D-69120 Heidelberg, Germany. E-mail: f.kiessling@dkfz.de

Received 27 October 2006; Revised 6 December 2006; Accepted 7 December 2006.

DOI 10.1593/neo.06688

Noninvasive imaging techniques have gained importance in the investigation of tumor growth and spread. Noninvasive optical imaging of stable transfected cell lines expressing fluorescent molecules is of high value in preclinical research [10,11]. Magnetic resonance imaging (MRI) is frequently used for the detection and staging of PCa in patients. Recent developments in MRI and magnetic resonance spectroscopy (MRS) have improved our understanding of tumor biology and have particularly enabled the detection and characterization of PCa and lymph node metastasis [12–14]. In this context, improved sensitivity and specificity for the detection of PCa were achieved by supplementing morphologic MRI with [^{1}H]NMR spectroscopic imaging [15,16] to assess tumor metabolism. Furthermore, dynamic contrast-enhanced MRI (DCE-MRI) is frequently used to characterize microcirculation in PCa [17,18]. It has been shown that even simple parameters describing signal time courses after injection of a contrast agent, such as the initial slope and the maximum of relative signal enhancement, assist in the differentiation between PCa and normal peripheral glands [18]. However, for a more precise analysis of tumor physiology, pharmacokinetic models providing quantitative data on regional blood volume (RBV), regional blood flow (RBF; perfusion), and capillary permeability are highly desirable. These parameters can be estimated, for example, by pharmacokinetic analysis of acquired DCE-MRI data using an open two-compartment model [19].

Clinical [^{1}H]MRS studies have demonstrated that signal intensities of the metabolites citrate (Ci; multiplet centered at chemical shift δ = 2.6 ppm), choline and choline-containing compounds (Cho; δ = 3.22 ppm), and creatine and phosphocreatine (Cr; δ = 3.03 ppm) provide a measure for the biochemical characterization of prostatic lesions ("CC/C value"). In the normal prostate, Ci is secreted and stored in the peripheral zone and, therefore, causes an intense signal in the [^{1}H]MR spectrum. In PCa, the Ci concentration, hence the corresponding [^{1}H]MR signal, often exhibits a decrease. An elevated Cho signal indicates increased membrane turnover and cell necrosis. Cr are related to the energy metabolism of cells and are useful for standardization because these metabolites usually do not increase in tumors. Thus, an increased amount of Cho typically found in tumors with high proliferative activity [20,21] and a decrease in Ci + Cr signal intensities have proven to be useful markers of PCa [15]. Lipid fractions, which are an indicator of cell degeneration (i.e., of necrosis and, therefore, possibly of anaplasia), have not been studied in PCa so far. However, a recent study on hepatocellular carcinomas indicated that dedifferentiation of liver lesions goes with an increase in the concentrations of free lipids [22]. Thus, lipid fractions are also a possible candidate for supplementing the grading of PCa.

However, up to now, it is uncertain whether DCE-MRI and [^{1}H]MRS are capable of assessing tumor aggressiveness [23–25]. In this context, the correct staging of PCa has been revealed to be complicated by the heterogeneous and multifocal nature of this tumor. Usually, there is no solitary PCa clone deriving from one tumor cell but a conglomerate of benign glandular structures, preneoplastic foci (prostatic intraepithelial neoplasia), and neoplastic foci with different grades of dedifferentiation [26]. These aspects of PCa have been considered in histologic Gleason grading, which proved to be an excellent prognostic indicator [27].

Based on these findings, we investigated the influence of tumor environment on the development of experimental prostate tumors with different malignancies in rats. Tumors were exposed to different microenvironments by orthotopic and subcutaneous implantations. Tumor growth, spread, microcirculation, and metabolism were evaluated by morphologic MRI, DCE-MRI, and [^{1}H]MRS, in combination with histopathological analysis.

Materials and Methods

Animals and Tumor Models

Experiments were performed with the approval of the institutional committee for animal research and in conformity with national guidelines for the care and use of laboratory animals.

As a tumor model for PCa, the original Dunning R3347 PCa of rats from J. T. Isaacs (John Hopkins, Baltimore, MD) was chosen, which spontaneously arose in a Copenhagen rat and was isolated from lymph node metastasis in 1963 [28]. Different sublines were drawn by repeated passaging in castrated rats. Their common characteristic is resemblance to human prostate carcinoma with respect to both histologic and enzymatic patterns [29,30].

In the present study, the well-characterized sublines H (hormone-sensitive), HI (hormone-insensitive), and AT1 were chosen for their different volume-doubling times, hormonal dependency, and histologic phenotype. The subtype H was observed to be highly differentiated and hormone-dependent, whereas the HI Dunning tumor was moderately differentiated, was insensitive to hormones, and produced mucin. The AT1 subline used as the third model forms anaplastic hormone-independent tumors without glandular differentiation. The volume-doubling time ranged from 20 days for subtype H, to 10 days for subtype HI, to 2.7 days for AT1 tumors. The three sublines exhibited a low metastatic potential in common [31].

A total of n = 49 adult male Copenhagen rats (body weight: ~ 180–200 g; age: 4–6 weeks) were included. Tumors of the three sublines were inoculated subcutaneously in the right hind leg using fragments of donor tumors with a volume of approximately 1 to 2 mm^3. Alternatively, tumor fragments were implanted orthotopically in the dorsolateral lobe of the prostate following a protocol described by Lein et al. [32,33] and Hahn et al. [34]. In our study, a higher number of orthotopic H tumor implantations were necessary due to a lower tumor take rate (Figure 1).

Anesthesia

For tumor inoculation and MR examinations, the rats were anesthetized by inhalation of a mixture of isoflurane (1.5%), N_2O (35%), and oxygen (60%). Tail vein was catheterized with a 26-gauge cannula (Abbott, Sligo, Ireland).

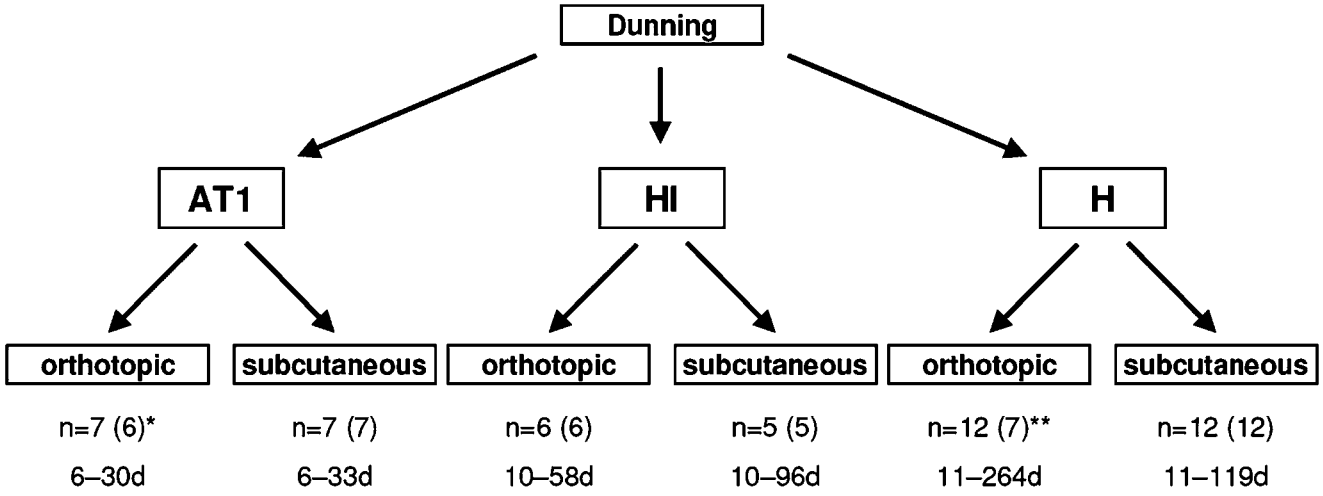

Figure 1. *Study plan. The study plan includes the number of animals in which H, HI, and AT1 tumors were implanted and the number of implantations that led to successful tumor growth (take rate in brackets). Bottom line: Time intervals of examinations with MRI.*

MRI

MRI was performed on a clinical 1.5-T whole-body MR system (Magnetom Symphony; Siemens Medical Solutions, Erlangen, Germany) using a home-built coil for radiofrequency excitation and detection, designed as a cylindrical volume resonator with an inner diameter of 83 mm and a usable length of 120 mm [17].

Animals with orthotopic tumors were examined with transversal and sagittal imagings, whereas those with subcutaneous tumors were examined with transversal and coronal T_2-weighted (T_{2w}) turbo spin echo (TSE) MR sequences according to the following protocols: transversal T_{2w} TSE: repetition time T_R = 3240 milliseconds, echo time T_E = 81 milliseconds, matrix size MA = 256 × 152, field of view (FOV) = 90 × 54 mm^2, slice thickness T_H = 1.5 mm; coronal T_{2w} TSE: T_R = 3240 milliseconds, T_E = 72 milliseconds, MA = 256 × 108, FOV = 150 × 63 mm^2, T_H = 2 mm; sagittal T_{2w} TSE: T_R = 3240 milliseconds, T_E = 78 milliseconds, MA = 255 × 88, FOV = 150 × 51 mm^2, T_H = 1 mm.

When tumors reached a diameter of approximately 5 mm, morphologic MRI was supplemented with DCE-MRI. On the basis of acquired T_{2w} images, two transversal sections were defined (T_H = 4.5 mm, FOV = 130 × 98 mm^2): one at the position of maximum tumor size, and the other at the heart level to determine the arterial input function from the left ventricle or the thoracic aorta. To estimate the precontrast longitudinal relaxation times (T_1) of blood and carcinoma, T_1-weighted (T_{1w}) images were acquired from predefined sections using a saturation–recovery Turbo FLASH sequence (T_R = 373 milliseconds, T_E = 1.76 milliseconds, flip angle α = 20°, MA = 192 × 144, FOV = 130 × 98 mm^2) with recovery times (T_{REC}) varying between 200 and 4000 milliseconds.

The same sequence was used for DCE-MRI, with T_R = 373 milliseconds, T_E = 1.76 milliseconds, T_{REC} = 130 milliseconds, α = 20°, and T_H = 4.5 mm. In total, 512 dynamic scans were acquired from both sections, with a temporal resolution of 0.6 s. Five seconds after starting DCE-MRI measurements, 200 μl (0.1 mmol/kg body weight) of the paramagnetic contrast agent Gd-DTPA-BMA (Omniscan; GE Healthcare, Munich, Germany) was injected manually within 2 seconds into the tail vein of rats. Finally, postcontrast high-resolution T_{1w} FLASH images covering the whole tumor region were obtained (T_R = 600 milliseconds, T_E = 14 milliseconds, MA = 144 × 256, FOV = 72 × 54 mm^2, α = 90°, T_H = 1.5 mm).

MRS

When subcutaneous tumors exhibited diameters larger than 5 mm, localized [^{1}H]MR spectra were obtained using an horizontal-bore (20 cm) animal spectrometer with B_0 = 9.4 T (9.4/20 BioSpec; Bruker BioSpin MRI GmbH, Ettlingen, Germany). Following T_{2w} MRI for tumor localization, single-voxel [^{1}H]MRS was performed [point-resolved spectroscopy (PRESS) with selective water signal suppression, T_R = 2000 milliseconds, T_E = 14 milliseconds, number of excitations = 128, voxel size = 4 × 4 × 4 mm^3] using a surface coil of 2 cm diameter. Three subcutaneous tumors of each subline were examined, and each tumor was measured thrice with the same sequence parameters for validation of intra-individual reproducibility. Attempts to acquire MR spectra from the prostate failed because of varying susceptibilities in the pelvis and markedly lower sensitivity of the surface coil to intraprostatic signals compared to subcutaneously implanted tumors.

Data Analysis

Tumor volumes were estimated by assuming ellipsoidal shapes from tumor diameters determined for three orthogonal directions from T_{2w} MR images. Due to the presence of large variations in growth rates between different sublines,

we relinquished to consider tumors that were grown for the same period of time, but rather compared tumors of similar sizes (at least 5 mm diameter) and lacking extended areas of necrosis.

For quantitative analysis of DCE-MRI data, MR signal time courses were determined from regions of interest defined over the central part of the right ventricle (or the aorta) and within each tumor. For each region, precontrast T_1 relaxation times were estimated by nonlinear regression analysis and used to convert measured signal time courses into concentration–time courses [19].

Individual concentration–time courses were analyzed using a pharmacokinetic two-compartment model [19], which described the transport of Gd-chelate through capillaries and its bidirectional transport between plasma and interstitial space. Using the program MKMODEL (version 5.0; Biosoft, Cambridge, UK), the permeability–surface area product per unit of vascular volume (PS/V_P), the RBV per unit tissue mass RBV (ml/100 g tissue), and the RBF per unit tissue mass RBF (ml/min/100 g tissue) were estimated [19,35]. For each group, means and standard deviations were calculated. Additionally, aggregated concentration–time courses of tumors were generated by averaging the individual concentration–time courses determined for six different groups (three sublines and two localizations).

In vivo [^{1}H]MRS data were postprocessed and displayed using the user interface jMRUI [36].

Histologic Evaluation

The rats were sacrificed when the tumor diameter exceeded 15 mm in subcutaneously implanted tumors and 10 mm in orthotopically implanted tumors.

For histologic phenotyping, tumors were dissected, covered with Tissue-Tek (Sakura, Zoeterwoude, The Netherlands), and frozen in liquid nitrogen vapor. Tumor sections with a thickness of 6 μm were cut using a Reichert-Jung Frigocut 2700 microtome (Leica, Bensheim, Germany). For histology, sections were stained with hematoxylin and eosin (HE).

Double-immunofluorescence images of endothelial cells and pericytes were generated using primary antibodies against PECAM-1 (mouse anti-rat anti-CD31 mAb, 1:50 concentration; Chemicon International, Temecula, CA) and rabbit anti-rat Ng-2 (rabbit anti-rat Ng-2 pAb; Chemicon International; 1:100 concentration), secondary TRSC-labeled antibodies against mouse IgG (1:100 concentration; Dianova, Hamburg, Germany), and Cy2-labeled antibodies against rabbit IgG (1:50 concentration; Dianova). Alternatively, staining of PECAM-1 was combined with that of smooth muscle actin (SMA). For this purpose, primary antibodies against SMA (rabbit anti-human anti–SMA pAb, 1:100 concentration; Biozol, Eching, Germany) and secondary Cy2-labeled antibodies against rabbit IgG (1:50 concentration; Dianova) were used.

Apoptotic cells were assessed by terminal deoxyribosyl transferase–mediated dUTP nick end labeling (TUNEL) staining (*In Situ* Cell Death Detection Kit, TMR red; Roche Diagnostics, Mannheim, Germany) performed according to the instructions of the manufacturer.

In all cases, additional counterstaining was performed using Hoechst nuclear staining (1:100 concentration; Invitrogen, Paisley, UK).

Tissue sections were viewed by phase-contrast microscopy, and images were captured with a digital camera (Color View 1; Soft Imaging System GmbH, Muenster, Germany). For fluorescence microscopy, a Leica microscope (DMRE, Bensheim, Germany) with an adapted digital camera (F-view XS; Soft Imaging System GmbH) was used. Quantitative analysis of marker density on histologic sections was performed by calculating positive area fractions using the Analysis Software (Soft Imaging System GmbH). In this context, at least three different tumors per model and implantation site were analyzed.

For each tumor, more than three different regions of interests were placed randomly. Because the tumors did not show marked central degradation, it was not necessary to analyze tumor margins and centers separately.

Statistical Analysis

Differences in parameters characterizing tumor size, vascularization, and immunohistology between groups were compared using Student's *t* test at a significant level of $P = .05$.

Results

Growth and Spread of PCa

In T_{2w} MR images, subcutaneous tumors were clearly identified as hyperintense relative to surrounding muscles, whereas orthotopic tumors appeared hypointense relative to normal prostate tissues. In both cases, a clear delineation of PCa from surrounding tissues and, thus, reliable determination of tumor diameters were feasible.

Subcutaneous tumor induction was successful in all H tumors ($n = 12$), HI tumors ($n = 5$), and AT1 tumors ($n = 7$). Orthotopic implantation of H sublines, however, succeeded in only 7 of 12 cases, but in all HI tumors ($n = 6$) and AT1 tumors ($n = 6$).

As expected from the characteristics of the tumor subtypes [31], the growth of tumors diverged and increased from H tumors, to HI tumors, to AT1 subtypes for both implantation sites. The comparison of orthotopic tumor growth and subcutaneous tumor growth indicated that H tumors grew significantly ($P < .05$) slower in the prostate than in subcutaneous localization (Figure 2). In contrast, the growth of orthotopic *versus* subcutaneous HI and AT1 tumors did not differ significantly, respectively. Surprisingly, in the case of orthotopic *versus* subcutaneous HI tumors, lymph node metastases were observed in four of six animals, whereas no metastasis was found for the other models.

Histologic Phenotypes

HE-stained histologic sections of H, HI, and AT1 tumors exhibited marked phenotypical differences (Figure 3). H tumors showed high stromal density and tubular structures similar to those found in normal prostate tissues. On the contrary, HI tumors tended to form irregular ring-like

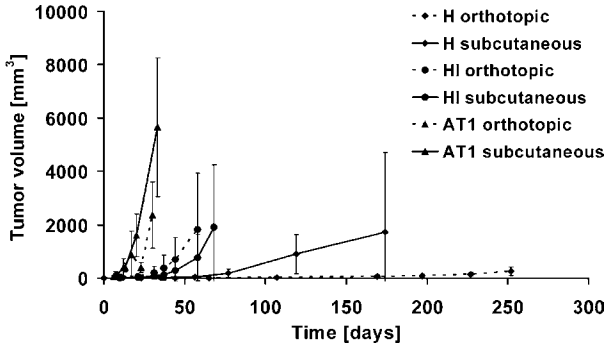

Figure 2. *Acceleration of tumor growth. Growth of H, HI, and AT1 tumors after orthotopic placement (closed line) and subcutaneous placement (dotted line). Differentiated H tumors showed the slowest growth rates, whereas anaplastic AT1 tumors displayed the fastest growth rates. Comparing tumor growth after orthotopic and subcutaneous implantations, orthotopic H tumors showed retarded growth ($P < .05$, starting on day 11), whereas orthotopic HI tumors exhibited accelerated growth. Differences in the growth rates of orthotopic and subcutaneous AT1 tumors were not significant. Note: The decline of the growth curve of orthotopic AT1 tumors on day 17 resulted from the removal of three animals with symptomatic disease.*

structures filled with large amounts of mucin, whereas AT1 tumors were found to be anaplastic without tubular structures. Thus, glandular differentiation was associated with slow tumor growth. In this context, immunohistologic analysis indicated that glandular differentiation was associated with a close interaction of tumor cells and smooth muscle cells (SMC). Accordingly, SMC fractions decreased from H tumors, to HI tumors, to AT1 tumors (Figures 4 and 5). SMC associated with mature vessels represented only a minor fraction in H tumors, but were dominant in HI and AT1 tumors.

Between orthotopic and subcutaneous HI and AT1 tumors, there was no obvious difference in histomorphology (Figures 4 and 5). In contrast, subcutaneously growing H tumors frequently showed dedifferentiated areas with polyploid tumor cells that were not visible in orthotopic locations. In addition, compared with subcutaneous ones, there was a significant decrease in the area fraction of SMC in orthotopic H tumors. Morphologically, this was reflected by

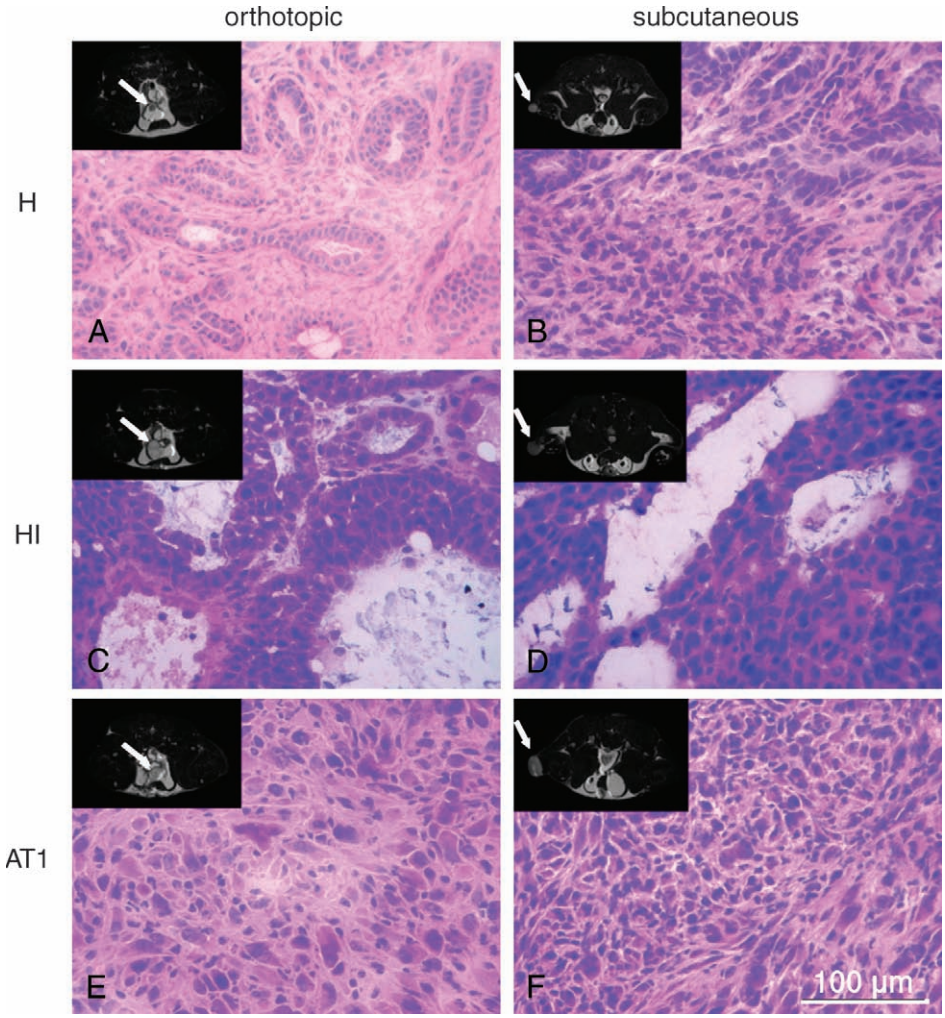

Figure 3. *HE staining of Dunning PCa. Images of HE-stained orthotopic tumors (A, C, E) and subcutaneous (B, D, F) H tumors (A and B), HI tumors (C and D), and AT1 tumors (E and F). The corresponding T_{2w} MR images are supplemented on the upper left part of each image. Tumors are labeled with arrows. The loss of differentiation from H tumors, to HI tumors, to AT1 tumors is visible. Orthotopic H tumors are highly differentiated and show tubular structures. (A) Dedifferentiated areas, however, are frequently found in subcutaneous H tumors. (B) HI tumors (C and D) secrete mucin, which is found in large lacunes mimicking tubular structures. AT1 tumors (E and F) have an anaplastic phenotype without distinct resemblance to the tissue of origin. Both HI tumors (C and D) and AT1 tumors (E and F) do not show marked differences for the two implantation sites. Bar = 100 μm.*

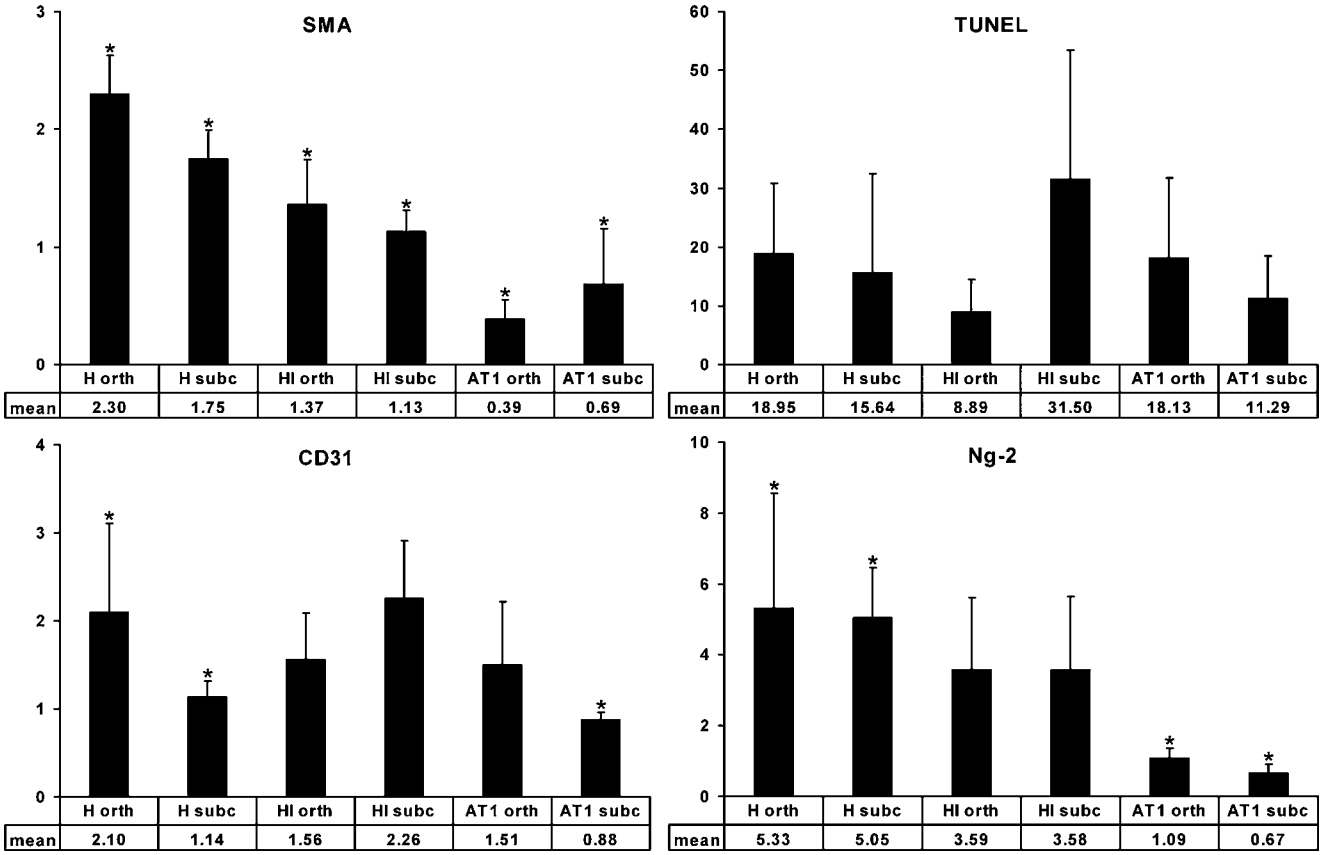

Figure 4. *Results from immunostaining. Plots of mean positive area fractions of SMA, TUNEL, CD31, and Ng-2 (± standard deviation) in orthotopic and subcutaneous PCa of H, HI, and AT1 sublines. SMA area fractions decreased from H tumors to AT1 tumors and have significantly higher values in orthotopic H tumors compared with all other tumors and subcutaneous H tumors with subcutaneous HI tumors and both AT1 tumors. Differences between orthotopic HI tumors and both AT1 tumors, as well as subcutaneous HI tumors and orthotopic AT1 tumors, were also significant. According to TUNEL staining, no significant differences were observed between the three tumor sublines in orthotopic and subcutaneous locations. Vessel density (CD31) was significantly higher in orthotopic H tumors as in subcutaneous H and AT1 tumors. Ng-2 decreased from H tumors, to HI tumors, to AT1 tumors without showing significant differences between the orthotopic and subcutaneous implantation sites of the same subline, but with significant decrease between both H tumors and both AT1 tumors. *P < .05.*

the frequently incomplete or absent surroundings of tubular tumor cell islets by SMC.

All tumor models showed a highly heterogeneous pattern of TUNEL staining (apoptosis) without significant differences between sublines and between orthotopic and subcutaneous tumors (Figures 4 and 5).

Vessel density, as determined by CD31 immunostaining, diverged between the different tumor models and implantation sites (Figures 4 and 5). A significantly higher vessel density was observed in orthotopic H tumors compared with subcutaneous ones ($P < .05$) and with subcutaneous AT1 tumors ($P < .01$). Cross correlation between the other conditions did not indicate significant differences. The area fractions of mature vessels, as indicated by Ng-2 immunostaining, decreased from H tumors to HI tumors to AT1 tumors. Significant differences were found for H and AT1 tumors in both implantation sites. However, the comparison of orthotopic and subcutaneous tumors did not indicate significant differences (Figures 4 and 5).

Assessment of Vessel Function by DCE-MRI

H, HI, and AT1 tumors could not be distinguished based on their RBV and permeability–surface area product (PS/V_p). In comparing orthotopic *versus* subcutaneous tumors, there were no significant differences according to these physiological parameters. RBF, however, was lower in orthotopic H tumors, such as in subcutaneous ones, and in HI tumors ($P < .05$) and AT1 tumors at both implantation sites. Furthermore, as a general tendency, cumulated concentration–time curves showed higher values for subcutaneous tumors of all sublines (Table 1, Figure 6).

Assessment of Tumor Metabolism by [^{1}H]MRS

Localized *in vivo* [^{1}H]MR spectra of subcutaneous tumors showed good reproducibility on comparison between the three repeated measurements (performed with the same experimental parameters and voxel positions) of the same tumor. In addition, for different subcutaneous tumors of the same subline, comparable spectra were obtained.

However, the spectral pattern of H, HI, and AT1 sublines examined in this study differed distinctly. As expected for anaplastic tumors with rapid membrane turnover [16], there was a distinct Cho peak (δ = 3.2 ppm) in AT1 tumors. The interpretation of resonances at 3.2 ppm in the H and HI spectra (Figure 7), however, was more complex because of the presence of a pair of lines resonating at 3.2 and

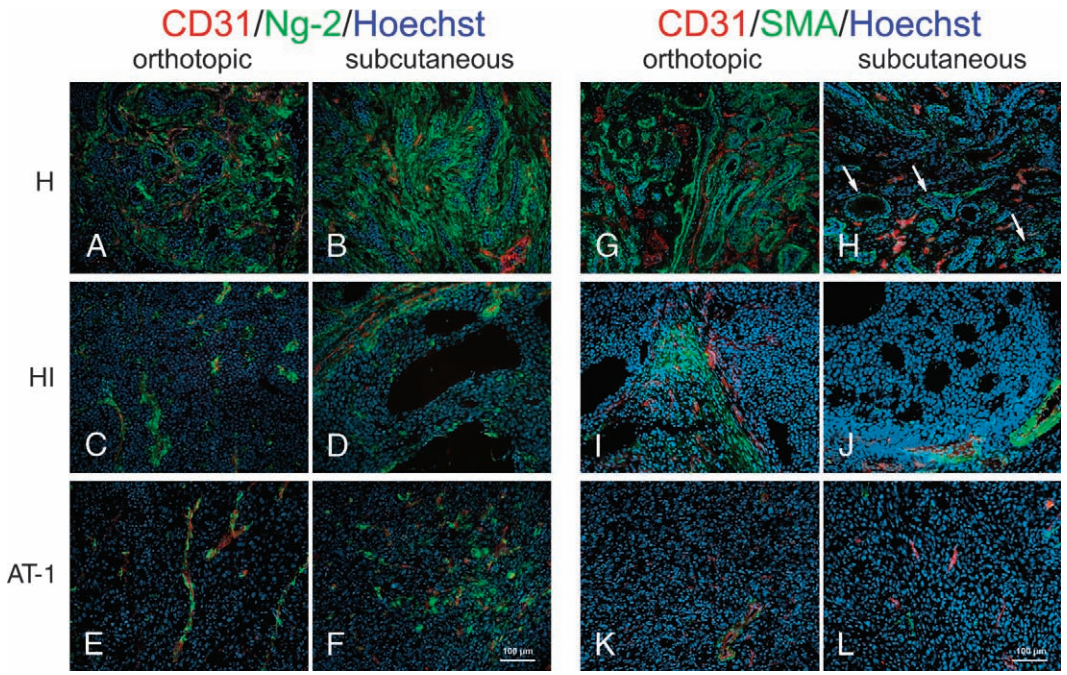

Figure 5. *Triple-immunofluorescence images of CD31, Ng-2, and DAPI of H, HI, and AT1 tumor sections. Ng-2 (green) colocalized with CD31-positive (red) vessels but could not be found on the surface of tumor cells. Furthermore, comparing H tumors (A and B) with HI tumors (C and D) and AT1 tumors (E and F) at both location sites, a significant decrease in the amount of Ng-2–positive vessels was observed. No significant difference was found on comparing subcutaneous and orthotopic tumors. The triple-immunofluorescence images of CD31 (red), SMA (green), and DAPI (blue) of H, HI, and AT1 tumor sections are shown in (G) to (L). In orthotopic H tumors, most SMAs localized around glandular tumor islets, and only minor amounts were associated with CD31-positive vessels. In subcutaneous H tumors, the association of SMC and tumor cells decreased, and the surroundings of tubular tumor cell specifications were frequently incomplete or absent (arrows). In HI and AT1 tumors, SMA was predominantly found along vascular structures, which is true for both implantation sites. Almost no direct association of glandular tumor cell islets and SMC could be observed. Bar = 100 μm.*

3.4 ppm, with the first one overlapping with the choline peak. According to measurements in model solutions at 7 T [37], these resonances (indeed two unresolved triplets) were attributed to taurine (Tau). Although the Cho intensity dominated in the AT1 tumor spectrum at 3.2 ppm, the corresponding signals in H and HI tumors originated mainly from Tau, as it is known to interact with SMC [38] and to reduce lipolysis [39].

Further inspection of Figure 7 showed that the signal intensity of unsaturated lipid fraction (free fatty acids and triacylglycerides; chemical shift range δ = 0.8–1.5 ppm) increased from differentiated H tumors to HI tumors to anaplastic AT1 tumors.

In summary, the results indicate that for differentiated H tumors, implantation site highly influences growth, whereas it is less relevant for highly dedifferentiated HI and AT1 tumors. Two major phenotypical differences were observed between orthotopic and subcutaneous H tumors. Firstly, the density of CD31-positive vessels was significantly increased in orthotopic H tumors. Secondly, the SMC density associated with tubular tumor cell islets was reduced in subcutaneous H tumors and in the more dedifferentiated HI and AT1 tumors. In this context, it might be interesting to

Table 1. Parameters of Tumor Vascularization (Mean ± Standard Deviation) Estimated from DCE-MRI Data Using an Open Two-Compartment Model.

	Permeability (PS/V_P) (l/min)	RBV (ml/100 g)	RBF (ml/min/100 g)
H orthotopic	1.6 ± 3.9	3.1 ± 2.8	63 ± 36
H subcutaneous	1.6 ± 1.3	2.2 ± 0.5	108 ± 35
HI orthotopic	1.8 ± 2.8	1.9 ± 0.6	109 ± 22
HI subcutaneous	1.0 ± 2.7	1.9 ± 0.5	145 ± 53
AT1 orthotopic	1.0 ± 3.5	3.1 ± 2.3	119 ± 110
AT1 subcutaneous	1.2 ± 2.8	2.2 ± 0.5	127 ± 79

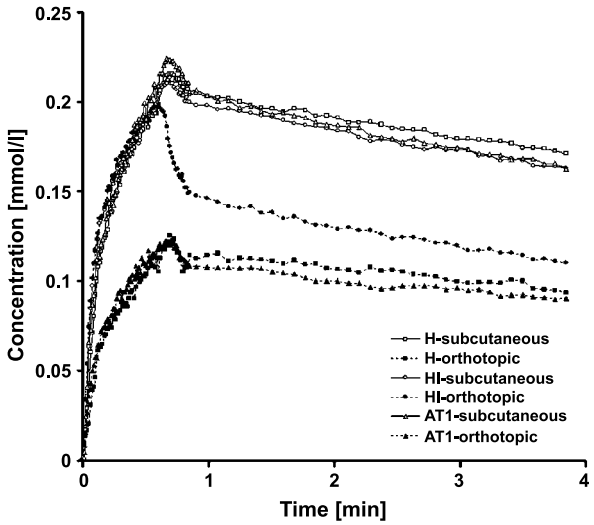

Figure 6. *Concentration–time courses from DCE-MRI. The concentration–time courses were averaged over tumors within each of the six groups. Higher concentrations of the contrast agent compared to their orthotopic counterparts are accumulated in subcutaneous tumors.*

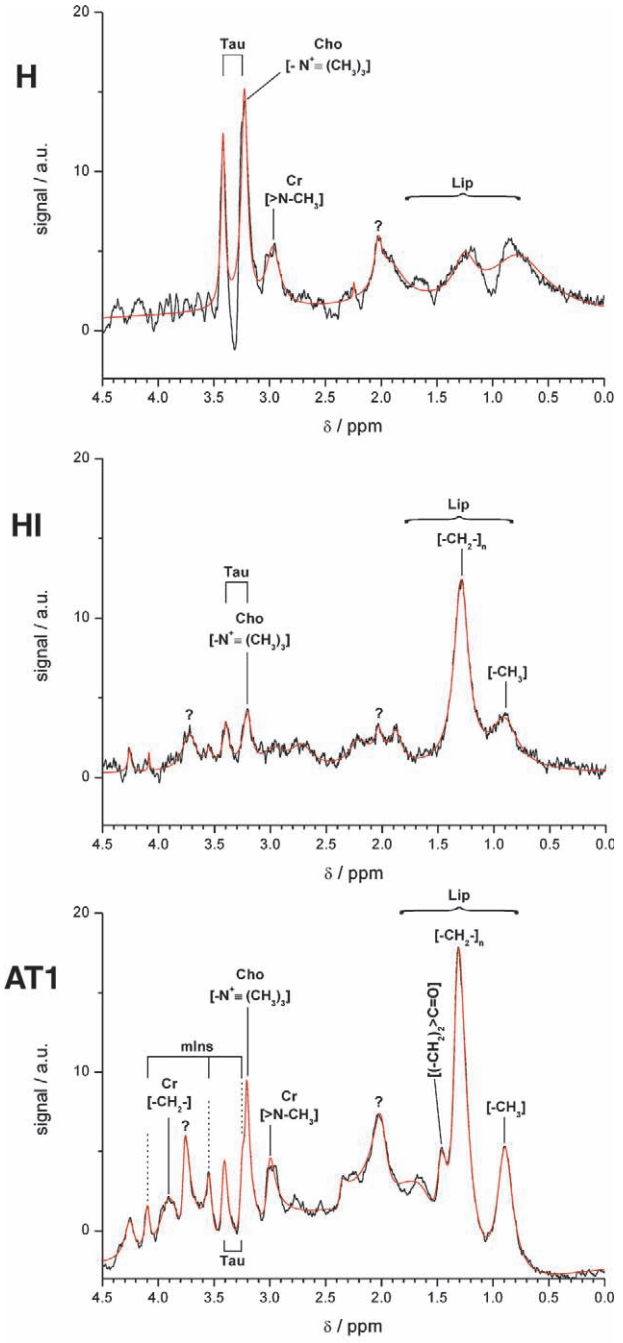

Figure 7. *[^{1}H]MRS of subcutaneous Dunning PCa. Localized* in vivo *[^{1}H]MR spectra of subcutaneous H, HI, and anaplastic AT1 tumors [PRESS technique: water signal suppression, T_R = 2000 milliseconds, T_E = 14 milliseconds, number of excitations = 128, voxel size = 4 × 4 × 4 mm^3, planar surface coil B_0 = 9.4 T]. The chemical shift scale (δ) could be fixed by identification of the peaks of >N-CH$_3$ protons of Cr (H and AT1) and of methylene and methyl protons of lipids (Lip) (HI and AT1). Analysis of the multiline spectrum of AT1 tumors yielded the signal of methylene protons of Cr at δ = 3.9 ppm, whereas the resonance at δ = 3.2 ppm appeared as a superposition of the N-trimethyl proton signal of Cho and a signal at about 3.25 ppm (shoulder at the low-field side). This signal, together with the peaks at δ = 3.52 and 4.1, was tentatively assigned to myo-inositol (mIns) using chemical shifts (δ = 3.28, 3.52, 3.62, and 4.06 ppm) measured at B_0 = 7.0 T for mIns model solution [37]. Inspection of the spectrum of H tumors led to the assignment of two peaks of equal intensity at about 3.2 ppm (with possible signal contribution of Cho) and 3.4 ppm (measured chemical shift difference: 0.17 ppm) to Tau when referring to shifts δ = 3.26 ppm (triplet) and 3.43 ppm (triplet) observed in a Tau model solution at B_0 = 7.0 T [37]. Tau was observed in all three spectra. The peaks at δ = 2.05 (resolved in all spectra) and 3.75 ppm (HI and AT1) with varying intensities could not be assigned unambiguously.*

know that [^{1}H]MRS indicated that H, HI, and AT1 tumors contained different amounts of Tau, which is known to play a role in the stabilization and differentiation of SMC. The possible association of these findings will be discussed in detail in the Discussion section.

Discussion

Our results from noninvasive imaging, in combination with histologic evaluation of experimental PCa, demonstrate several novel findings on the influence of microenvironment on the PCa phenotype: 1) the growth of highly differentiated H tumors was influenced by implantation site; 2) influence seemed less important for the development of intermediate malignant HI tumors and anaplastic AT1 tumors; 3) in orthotopic H tumors, SMC had a close interaction with glandular tumor islets, which was reduced in subcutaneous H tumors and was almost absent in HI and AT1 tumors; 4) microcirculatory parameters estimated from DCE-MRI data did not show significant differences between tumor types, whereas higher perfusion values were observed in all subcutaneous tumors compared to orthotopic ones; 5) microvessel density was increased in orthotopic H tumors compared with subcutaneous ones and other models at both implantation sites; 6) the amount of mature vessels decreased from H tumors, to HI tumors, to AT1 tumors; and 7) [^{1}H]MRS indicated a decrease in Tau and an increase in lipid components from low to high malignant tumors.

These observations may point to an important mechanism of PCa dedifferentiation and to the need of tumor models grown in an adequate microenvironment. From various tumors [40], such as bladder carcinomas [41], colon carcinomas [42], renal carcinomas [43], and PCa [44], it is already known that the tumor phenotype and its metastatic potential are different between orthotopic and subcutaneous tumors. In addition, using the Dunning AT3 PCa model, different routes of systemic spread were described for orthotopically and subcutaneously grown tumors [45]. Subcutaneous tumors grown in the flank exhibited lung metastases, whereas those grown in the prostate metastasized locally. They also displayed a higher take rate when implanted orthotopically. In contrast, in our study, highly differentiated H tumors had a lower take rate and slower growth when implanted orthotopically, whereas HI and AT1 tumors grew in both locations comparably (Figure 1). However, in HI tumors, we detected macroscopic lymph node metastases only after orthotopic implantation, which is in line with the findings of Glinskii et al. [44] describing the presence of circulating tumor cells of PC-3 PCa in nude mice only after orthotopic implantation.

Significant differences in growth were observed between subcutaneous and orthotopic H tumors. The H tumor subline represents an experimental tumor quite similar to that found in humans, and there are several studies dealing with hormone dependence and growth pattern. Although Lubaroff and Culp [46] reported glandular differentiation both for orthotopic and subcutaneous tumors, we regularly found dedifferentiated islets only in H tumors grown subcutaneously.

These may be derived from new tumor cell mutations occurring during the growth of tumors or from the preexisting 8% to 30% HI cells, which have been described by Smolev et al. [47] to initiate growth soon after castration.

Under normal conditions, androgen-dependent stromal cells play a crucial role in maintaining a fully differentiated growth-quiescent gland. It is also known that prostatic carcinogenesis is associated with changes in interactions between the stromal microenvironment and tumor cells [7,48]. In this context, Cunha et al. [7] found progressive loss of SMC and appearance of carcinoma-associated fibroblasts. Thus, slow growth and high differentiation of orthotopic H tumors might have been preserved by a close interaction with stromal cells. The growth of hormone-independent HI and anaplastic AT1 tumors, however, may depend, to a lesser extent, on implantation site due to minor requirements for stromal interaction and better adaptation to varying implantation sites caused by clonal mutation and selection [7]. Here, malignant stroma may contribute more for maintaining the three-dimensional tumor architecture [49] than for keeping a differentiated tumor phenotype.

Tumor growth and differentiation strongly depend on blood supply, vascularization, and angiogenesis [50–52]. Accordingly, in our models, significant differences in tumor vascularization were observed. A decrease in mature vessel fractions from H tumors, to HI tumors, to AT1 tumors was observed, which is in line with previous observations describing a negative correlation of tumor malignancy with vessel maturity for different tumor entities [53]. However, orthotopic H tumors developed the highest vessel density of all models and presented a higher density of Ng-2–positive mature vessels than AT1 and HI tumors. The observation of a higher vessel density in orthotopic Dunning PCa is in line with the findings of Chen et al. [54], who found a higher total vessel density in anaplastic MatLyLu-Dunning carcinomas grown in the prostate compared with subcutaneous tumors. However, it remains uncertain why, in our study, this was only true for differentiated H tumors, whereas for highly dedifferentiated HI and AT1 tumor models, we did not observe significant differences in vessel density between orthotopic and subcutaneous tumors. Besides the influence of the local microenvironment on tumor angiogenesis, the high vessel density (CD31) and the high fraction of Ng-2–positive mature vessels observed in low malignant orthotopic H tumors may also be explained by slow tumor growth, giving tumors more time to develop a stable and functional vascularization [55,56].

Surprisingly, orthotopic H tumors showed perfusion lower than those of subcutaneous ones and HI and AT1 tumors, independent of their implantation site. An explanation as to why higher vessel density may not go along with increased RBV and perfusion is that a relevant amount of tumor blood vessels, which are evaluated histologically, may not functionally contribute to tumor blood supply [57]. Mature vascularization with a lower frequency of vascular shunts may be another explanation for the reduced perfusion in orthotopic H tumors. Furthermore, histologic evaluation does not consider the quality of feeding and draining host vessels and the level of interstitial pressure [52,58]. Thus, recruitment of host blood and lymphatic vessels from different host tissues may be variable, and its resulting consequences on interstitial pressure may also explain changed tumor perfusion. This hypothesis is strengthened by the fact that all sublines exhibited lower perfusion in orthotopic implantation sites.

A high number of metabolites of low molecular mass were detected in tumors *in vivo* using high-resolution [^{1}H]MRS at 9.4 T. Firstly, the concentration of free fatty acids increased from highly differentiated H tumors to less differentiated HI to AT1 tumors. This is in agreement with findings in hepatocellular carcinogenesis [22] and may result from increasing amounts of free lipids, owing to aggravated lipolysis in tumors, enhanced membrane turnover, and the development of micronecrosis. Secondly, a significant increase in the level of Cho (mainly phosphocholine and glycerophosphorylcholine) as intermediates of membrane synthesis and degradation was observed in anaplastic AT1 tumors, which is in line with the clinical findings on PCa, brain tumors, and other neoplasias [59]. In contrast, in H and HI tumors, major contributions to the peak at δ = 3.2 ppm were assigned to Tau, and the amount rose in contrasting ranges of lipid components from AT1 tumors, to HI tumors, to H tumors. Tau is known to decrease lipid peroxidation and can reverse the contractile dysfunction of SMC [39]. Moreover, Tau restores the secretion and expression of extracellular superoxide dismutase, a glycoprotein secreted from vascular SMC [38]. Darnowski et al. [60] found a mechanism by which taurolidine, a derivate of Tau, caused cell death by apoptosis; therefore, Jacobi et al. [61] were successful in pointing out the anticancerogenic and antiangiogenic effects of taurolidine. Apoptosis indicated by TUNEL staining, however, was not shown to increase in our tumor models with high Tau levels.

Taking into account the data from the literature and our findings, we postulate that the levels of Tau in PCa may have an impact on tumor malignancy by modulating the interaction of tumor and SMC, which seems to be a prerequisite for differentiated phenotype. However, these findings have to be validated on PCa specimens of patients to elucidate whether the association of SMC with tumor cells and the levels of Tau and lipids in PCa can be used as diagnostic indicators of tumor malignancy.

References

[1] Rich AR (1935). On the frequency of occurrence of occult carcinoma of the prostate. *J Urol* **33,** 215–223.
[2] Yatani R, Chigusa I, Akazaki K, Stemmermann GN, Welsh RA, and Correa P (1982). Geographic pathology of latent prostatic carcinoma. *Int J Cancer* **29,** 611–616.
[3] Silverberg E and Lubera JA (1989). Cancer statistics 1989. *CA Cancer J Clin* **39,** 3–30.
[4] Etzioni R, Penson DF, Legler LM, di Tommaso D, Boer R, Gann PH, and Feuer EJ (2002). Overdiagnosis due to prostate-specific-antigen screening: lesson from US prostate cancer incidence trend. *J Natl Cancer Inst* **94,** 981–990.
[5] Nelson WG, De Marzo AM, and Isaacs WB (2003). Prostate cancer. *N Engl J Med* **349,** 366–381.
[6] Tenta R, Sotiriou E, Pitulis N, Thyphronitis G, and Koutsilieris M (2005). Prostate cancer cell survival pathways activated by bone metastasis microenvironment. *J Musculoskelet Interact* **5,** 135–144.
[7] Cunha GR, Hayward SW, and Wang YZ (2002). Role of stroma in carcinogenesis of the prostate. *Differentiation* **70,** 473–485.

[8] Tuxhorn JA, McAlhany SJ, Dang TD, Ayala GE, and Rowley DR (2002). Stromal cells promote angiogenesis and growth of human prostate tumors in a differential reactive stroma (DRS) xenograft model. *Cancer Res* **62,** 3298–3307.

[9] Hayward SW, Wang Y, Cao M, Hom YK, Zhang B, Grossfeld GD, Sudilovsky D, and Cunha GR (2001). Malignant transformation in a nontumorigenic human prostatic epithelial cell line. *Cancer Res* **61,** 8135–8142.

[10] Yang M, Jiang P, Yamamoto N, Li L, Geller J, Moossa AR, and Hoffman RM (2005). Real-time whole-body imaging of an orthotopic metastatic prostate cancer model expressing red fluorescent protein. *Prostate* **62,** 374–379.

[11] Yang M, Jiang P, Sun FX, Hasegawa S, Baranov E, Chishima T, Shimada H, Moossa AR, and Hoffman RM (1999). A fluorescent orthotopic bone metastasis model of human prostate cancer. *Cancer Res* **59,** 781–786.

[12] Barentsz JO, Engelbrecht M, Jager GJ, Witjes JA, de LaRosette J, van DerSanden BP, Huisman HJ, and Heershap A (1999). Fast dynamic gadolinium-enhanced MR imaging of urinary bladder and prostate cancer. *J Magn Imaging* **10,** 295–304.

[13] Harisinghani MG, Barentsz J, Hahn PF, Deserno WM, Tabatabaei S, van de Kaa CH, de la Rosette J, and Weissleder R (2003). Noninvasive detection of clinically occult lymph node metastases in prostate cancer. *N Engl J Med* **348,** 2491–2499.

[14] Beyersdorff D, Taupitz M, Winkelmann B, Fischer T, Lenk S, Loening SA, and Hamm B (2002). Patients with a history of elevated prostate-specific-antigen levels and negative transrectal US-guided quadrant or sextant biopsy results: value of MR imaging. *Radiology* **224,** 701–706.

[15] Scheidler J, Hricak H, Vigneron DB, Yu KK, Sokolov DL, Huang LR, Zaloudek CJ, Nelson SJ, Carrol PR, and Kurhanewicz J (1999). Prostate cancer. Localization with three-dimensional proton MR spectroscopic imaging—clinicopathologic study. *Radiology* **213,** 473–480.

[16] Kurhanewicz J, Vigneron DB, Hricak H, Narayan P, Carroll PR, and Nelson SJ (1996). Three-dimensional H-1 MR spectroscopic imaging of the *in situ* human prostate with high (0.24–0.7 cm^3) spatial resolution. *Radiology* **198,** 795–805.

[17] Kiessling F, Heilmann M, Vosseler S, Lichy M, Krix M, Fink C, Kiessling I, Steinbauer H, Schad L, Fusenig NE, et al. (2003). Dynamic T_1-weighted monitoring of vascularization in human carcinoma heterotransplants by magnetic resonance imaging. *Int J Cancer* **104,** 113–120.

[18] Kiessling F, Lichy M, Grobholz R, Heilmann M, Farhan N, Michel MS, Trojan L, Ederle J, Abel U, Kauczor HU, et al. (2004). Simple models improve the discrimination of prostate cancers from the peripheral gland by T_1-weighted dynamic MRI. *Eur Radiol* **14,** 1793–1801.

[19] Brix G, Kiessling F, Lucht R, Darai S, Wasser K, Delorme S, and Griebel J (2004). Microcirculation and microvasculature in breast tumors: pharmacokinetic analysis of dynamic MR image series. *Magn Reson Med* **52,** 420–429.

[20] Kurhanewicz J, Vigneron DB, and Nelson SJ (2000). Three-dimensional magnetic resonance spectroscopic imaging of brain and prostate cancer. *Neoplasia* **2,** 166–189.

[21] Beresford M, Padhani AR, Goh V, and Makris A (2005). Imaging breast cancer response during neoadjuvant systemic therapy. *Expert Rev Anticancer Ther* **5,** 893–905.

[22] Tesiram YA, Saunders D, and Towner RA (2005). Application of proton NMR spectroscopy in the study of lipid metabolites in a rat hepatocarcinogenesis model. *Biochim Biophys Acta* **1737,** 61–68.

[23] Kuhl CK, Mielcareck P, Klaschik S, Leutner C, Wardelmann E, Giesecke J, and Schild HH (1999). Dynamic breast MR imaging: are signal intensity time course data useful for differential diagnosis of enhancing imaging? *Radiology* **211,** 101–110.

[24] Stomper PC, Herman S, Klippenstein DL, Winston JS, Edge SB, Arredondo MA, Mazurchuk RV, and Blumenson LE (1995). Suspect breast lesions: findings at dynamic gadolinium-enhanced MR imaging correlated with mammographic and pathologic features. *Radiology* **197,** 387–395.

[25] Schlemmer HP, Merkle J, Grobholz R, Jaeger T, Michel MS, Werner A, Rabe J, and van Kaick G (2004). Contrast-enhanced dynamic MR imaging for the assessment of microvessel density in prostate cancer. *Eur Radiol* **14,** 309–317.

[26] Macintosh CA, Stower M, Reid N, and Maitland NJ (1998). Precise microdissection of human prostate cancers reveals genotypic heterogeneity. *Cancer Res* **58,** 23–28.

[27] Gleason DF (1992). Histologic grading of prostate cancer: a perspective. *Hum Pathol* **23,** 273–279.

[28] Dunning WF (1963). Prostate cancer in the rat. Biology of the prostate and related tissues. *Natl Cancer Inst Monogr* **12,** 351–369.

[29] Isaacs JT, Isaacs WB, and Coffey DS (1979). Models for the development of non-receptor methods for distinguishing androgen sensitive and insensitive prostatic tumors. *Cancer Res* **39,** 2652–2659.

[30] Isaacs JT and Coffey DS (1983). Model systems for the study of prostate cancer. In *Clinics in Oncology 2*. DP Murphy (Ed). W. B. Saunders, New York, pp 479–498.

[31] Isaacs JT, Heston WDW, Weissman RM, and Coffey DS (1978). Animal model of hormone sensitive and insensitive prostatic adenocarcinomas: Dunning R-3327-H, R-3327-HI, and R-3327-AT1. *Cancer Res* **38,** 4353–4359.

[32] Lein M, Jung K, Le DK, Hasan T, Ortel B, Borchert D, Winkelmann B, Schnorr D, and Loenings SA (2000). Synthetic inhibitor of matrix metalloproteinases (batimastat) reduces prostate cancer growth in an orthotopic rat model. *Prostate* **43,** 77–82.

[33] Lein M, Koenig F, Misdraji J, McDougal WS, Jung K, Loening SA, Hasan T, and Ortel B (2000). Laser-induced hyperthermia in rat prostate cancer: role of site of tumor implantation. *Urology* **56,** 167–172.

[34] Hahn EW, Peschke P, Mason RP, Babcock EE, and Antich PP (1993). Isolated tumor growth in a surgically formed skin pedicle in the rat: a new tumor model for NMR studies. *Magn Reson Imaging* **11,** 1007–1017.

[35] Brix G, Bahner M, Hoffmann U, Horvath A, and Schreiber W (1999). Regional blood flow, capillary permeability, and compartment volumes: measurement with dynamic computed tomography—initial experience. *Radiology* **210,** 269–276.

[36] Naressi A, Couturier C, Devos JM, Janssen M, Mangeat C, De Beer R, and Graveron-Demilly D (2001). Java-based graphical user interface for the MRUI quantitation package. *MAGMA* **12,** 141–152 (http://www.mrui.uab.es/mrui/).

[37] Michaelis T, Merboldt KD, Hanicke W, Gyngell ML, Bruhn H, and Frahm J (1991). On the identification of cerebral metabolites in localized ^{1}H NMR spectra of human brain *in vivo*. *NMR Biomed* **4,** 90–98.

[38] Nonaka H, Tsujino T, Watari Y, Emoto N, and Yokoyama M (2001). Taurine prevents the decrease in expression and secretion of extracellular superoxide dismutase induced by homocysteine: amelioration of homocysteine-induced endoplasmic reticulum stress by taurine. *Circulation* **104,** 1165–1170.

[39] Sener G, Ozer Sehirli A, Ipci Y, Cetinel S, Cikler E, Gedik N, and Alican I (2005). Taurine treatment protects against chronic nicotine-induced oxidative changes. *Fundam Clin Pharmacol* **19,** 155–164.

[40] Hoffman RM (1999). Orthotopic metastatic mouse models for anticancer drug discovery and evaluation: a bridge to the clinic. *Invest New Drugs* **17,** 343–359.

[41] Fu X and Hoffman RM (1992). Human RT-4 bladder carcinoma is highly metastatic in nude mice and comparable to ras-H–transformed RT-4 when orthotopically implanted as histologically intact tissue. *Int J Cancer* **51,** 989–991.

[42] Willmanns C, Fan D, O'Brian CA, Bucana CD, and Fidler IJ (1992). Orthotopic and ectopic organ environments differentially influence the sensitivity of murine colon carcinoma cells to doxorubicin and 5-fluorouracil. *Int J Cancer* **52,** 98–104.

[43] An Z, Jiang P, Wang X, Moossa AR, and Hoffman RM (1999). Development of a high metastatic orthotopic model of human renal cell carcinoma in nude mice: benefits of fragment implantation compared to cell-suspension injection. *Clin Exp Metastasis* **17,** 265–270.

[44] Glinskii AB, Smith BA, Jiang P, Li XM, Yang M, Hoffman RM, and Glinsky GV (2003). Viable circulating metastatic cells produced in orthotopic but not ectopic prostate cancer models. *Cancer Res* **63,** 4239–4243.

[45] Rubenstein M, Saffrin R, Shaw M, Muchnik S, and Guinan P (1995). Orthotopic placement of the Dunning R3327 AT-3 prostate tumor in the Copenhagen × Fischer rat. *Prostate* **27,** 148–153.

[46] Lubaroff DM and Culp DA (1977). Experience with an animal model for the study of prostatic carcinoma. *Trans Am Assoc Genitourin Surg* **69,** 72–77.

[47] Smolev JK, Coffey DS, and Scott WW (1977). Experimental models for the study of prostatic adenocarcinoma. *J Urol* **118,** 216–220.

[48] Arnold JT and Isaacs JT (2002). Mechanisms involved in the progression of androgen-independent prostate cancers: it is not only the cancer cell's fault. *Endocr-Relat Cancer* **9,** 61–73.

[49] Wang X, An Z, Geller J, and Hoffman RM (1999). High-malignancy orthotopic nude mouse model of human prostate cancer LNCaP. *Prostate* **39,** 182–186.

[50] Folkman J and D'Amore PA (1996). Blood vessel formation: what is its molecular basis? *Cell* **87,** 1153–1155.

[51] Jain RK (2003). Molecular regulation of vessel maturation. *Nat Med* **9,** 685–693.

[52] Vaupel P (2004). The role of hypoxia-induced factors in tumor progression. *Oncologist* **9** (5), 10–17.
[53] Hobbs SK, Monsky WL, Yuan F, Roberts WG, Griffith L, Torchilin VP, and Jain RK (1998). Regulation of transport pathways in tumor vessels: role of tumor type and microenvironment. *Proc Natl Acad Sci USA* **95,** 4607–4612.
[54] Chen B, Pogue BW, Zhou X, O'Hara JA, Solban N, Demidenko E, Hoopes PJ, and Hasan T (2005). Effect of tumor host microenvironment on photodynamic therapy in a rat prostate tumor model. *Clin Cancer Res* **11,** 720–727.
[55] Hlatky L, Hahnfeldt P, and Folkman J (2002). Clinical application of antiangiogenic therapy: microvessel density, what it does and does not tell us. *J Natl Cancer Inst* **94,** 883–893.
[56] Miller JC, Pien HH, Sahani D, Sorensen AG, and Thrall JH (2005). Imaging angiogenesis: applications and potential for drug development. *J Natl Cancer Inst* **97,** 172–187.
[57] Helmlinger G, Netti PA, Lichtenbeld HC, Melder RJ, and Jain RK (1997). Solid stress inhibits the growth of multicellular tumor spheroids. *Nat Biotechnol* **15,** 778–783.
[58] Jain RK and Fenton BT (2002). Intratumoral lymphatic vessels: a case of mistaken identity or malfunction? *J Natl Cancer Inst* **94,** 417–421.
[59] Schlemmer HP, Bachert P, Herfarth KK, Zuna I, Debus J, and van Kaick G (2001). Proton MR spectroscopic evaluation of suspicious brain lesions after stereotactic radiotherapy. *Am J Neuroradiol* **22,** 1316–1324.
[60] Darnowski JW, Goulette FA, Cousens LP, Chatterjee D, and Calabresi P (2004). Mechanistic and antineoplastic evaluation of taurolidine in the DU145 model of human prostate cancer. *Cancer Chemother Pharmacol* **54,** 249–258.
[61] Jacobi CA, Menenakos C, and Braumann C (2005). Taurolidine—a new drug with anti-tumor and anti-angiogenic effects. *Anticancer Drugs* **16,** 917–921.